Multichannel FT-Raman Spectroscopy: Noise Analysis and Performance Assessment

JUN ZHAO and RICHARD L. McCREERY*

Department of Chemistry, The Ohio State University, 100 West 18th Ave., Columbus, Ohio 43210

A Raman spectrometer based on forming an interferogram on a charge-coupled device (CCD) detector is evaluated further with respect to signal-to-noise ratio (SNR), stability, response correction, and resolution. The multichannel Fourier transform technique differs fundamentally from dispersive spectrometers and FT-Raman systems based on Michelson interferometers. Changes in entrance optics permitted multitrack operation and an improvement in collection efficiency. Both hardware and a more facile software procedure were examined for correction of noise caused by nonuniformity of the CCD response. The instrumental linewidth (ILW) for the multichannel Fourier transform (MCFT) system examined here was 14 cm^{-1} (full width at half-maximum), close to the 13.5 cm^{-1} predicted theoretically. An optical heterodyne method was used to downshift the observed Raman features and further reduce the ILW to 8 cm^{-1}. The unheterodyned MCFT spectrometer has a lower SNR than do dispersive systems for most samples, but has the advantages of frequency precision and large throughput. Several applications of MCFT are discussed, including examination of photolabile samples, multiple sample monitoring with fiber optics, and identification of MCFT spectra with a dispersive library.

Index Headings: **Raman spectroscopy; Fourier transform; Multichannel detectors, FT-Raman.**

INTRODUCTION

The rapid development of Raman instrumentation in the past ten years has progressed along two paths: spectrometers based on Michelson interferometers (FT-Raman)[1–3] and dispersive spectrometers with charge-coupled device (CCD) detectors.[4,5] The two developments have resulted in a rapid growth of applications of Raman spectroscopy in chemical analysis, as well as in fundamental research. In an initial report,[6] we discussed a combination of interferometric techniques and CCD detection, based on the formation of an interferogram on the face of a CCD array detector. The reported multichannel Fourier transform (MCFT) Raman spectrometer had no moving parts and provided full spectral coverage, low power density at the sample, and excellent frequency precision. In many applications, MCFT Raman spectroscopy combines the benefits of an interferometer with those of CCDs, leading to a possibly quite useful alternative to dispersive/CCD and FT-Raman approaches.

The concept of MCFT spectroscopy is at least 30 years old, with Stroke and Funkhouser reporting a device based on photographic detection.[7] Three configurations that produce an interferogram in space rather than in time have been described in the literature. One is based on a Michelson interferometer with a tilted rather than a scanning mirror.[8] The second type utilizes a Savart plate interferometer and two polarization filters,[9,10] and the third a Sagnac interferometer.[11–13] All three types are solid state and have no moving parts, but the Sagnac type has attracted the most attention, possibly due to its superior mechanical stability as compared with the Michelson type, and its more straightforward data processing as compared to the Savart plate type. Simultaneous recording of the interferograms in space has been achieved by using photographic film,[7] photodiode arrays,[11,14] and CCDs.[6,10,13] Takahashi et al.[10] described a Sagnac interferometer and CCD spectrometer for Raman spectroscopy, with the objective of minimizing laser power density in pulsed experiments. In a recent paper,[6] we described an MCFT Raman spectrometer based on a Sagnac interferometer and a 1024-channel CCD detector. This spectrometer was demonstrated to have superior stability, simplicity, and accuracy, large throughout, and sensitivity comparable to that of a multichannel dispersive Raman spectrometer.

The current paper reports significant instrumental improvements to our previous MCFT spectrometer, plus several important theoretical considerations and performance evaluations. These efforts address three specific issues: theoretical limits on signal-to-noise ratio (SNR) and resolution, improvements in instrumental design directed toward noise reduction, and use of an optical heterodyne technique for improving resolution.

THEORY

Signal-to-Noise Ratio of MCFT. The SNRs for dispersive/CCD[5] and FT-Raman spectrometers[1,15,16] have been described in detail and in both cases depend on several experimental conditions, including the laser power density, the sample area (or volume) monitored by the spectrometer (A_D), the detector quantum efficiency (Q), and the contributions from detector dark or readout noise. We will consider a sample illuminated by a uniform laser beam that overfills the spectrometer and generates Raman scattering with a specific intensity of L (photons s^{-1} cm^{-2} sr^{-1}). For the case of a dispersive/CCD system with negligible detector noise (and operating in the sample shot noise limit), the signal, S, and SNR are given by Eqs. 1 and 2.

$$S_{DIS} = L_i A_D \Omega Q T t_M, \quad (1)$$

$$SNR_{DIS} = (L_i A_D \Omega Q T t_M)^{1/2}_{DIS}. \quad (2)$$

L_i is the specific intensity in a particular spectral resolution element, T and Q are spectrometer transmission and quantum efficiency, Ω is the collection angle at the sample, and $A_D\,\Omega$ is often called the etendue.[5] t_M is the total measurement time, equal to the CCD integration time in this case. Since t_M is N_R (N_R = number of resolution elements) times as large as the single-channel measure-

Received 15 January 1997; accepted 30 May 1997.

* Author to whom correspondence should be sent.

0003-7028/97/5111-1687$2.00/0

ment time for a scanning spectrometer, a multichannel advantage of $N_R^{1/2}$ results, meaning that the SNR for the dispersive/CCD system is $N_R^{1/2}$ times as large as that for a scanning single-channel system with the same L, $A_D\,\Omega$, Q, and total measurement time.

Conventional FT-Raman spectrometers are often detector noise limited, with the multiplex nature of the interferometer partly compensating for a noisy detector. Equation 3 applies in the common case of the detector dark noise limit.

$$\mathrm{SNR_{FT}} = \frac{(L_i A_D \Omega Q T)_{FT} t_M^{1/2}}{\Phi_d^{1/2}} \tag{3}$$

where Φ_d is the dark count rate in electrons/s. The "multiplex advantage" stems from the fact that all wavelengths are monitored simultaneously, leading to an $N_R^{1/2}$ higher SNR than that of a single-channel system under the same noise conditions (due to longer t_M for each wavelength).

It is well established that the SNR characteristics of FT-Raman change significantly when the detector noise becomes smaller than or comparable to the sample shot noise, since the shot noise from the entire spectrum contributes to the noise at every wavelength. If more than one wavelength (or Raman shift) is monitored, a "multiplex disadvantage" results, which decreases the SNR in comparison to that for a multichannel instrument. Everall and Howard[15] examined the effect of shot noise on $\mathrm{SNR_{FT}}$ by considering the noise to be related to the square root of the total radiant power incident on the sample, which in turn is the number of resolution elements times the average power per resolution element. This relation is restated for the case of a shot-noise-limited FT-Raman experiment in Eq. 4, with the signal expressed in terms of electrons rather than radiant power:

$$\mathrm{SNR_{FT}} = \frac{S_i}{(\Sigma S_i)^{1/2}} = \frac{L_i}{(\Sigma L_i)^{1/2}} (A_D \Omega Q T t_M)_{FT}^{1/2}. \tag{4}$$

S_i represents the signal (e^-) for a given resolution element. Note that if only one resolution element contains signal, $\mathrm{SNR_{FT}}$ equals $\mathrm{SNR_{DIS}}$ if all else is equal. However, if many resolution elements contain signal, such as the case of a high background or a complex spectrum, $\mathrm{SNR_{FT}}$ decreases. Note also that the ($A_D\,\Omega\,TQ$) product can differ significantly for different instruments. This so-called "Fellgett disadvantage" can be partially compensated for by the larger $A_D\Omega$ of the Michelson interferometer used in conventional FT-Raman, compared to that of a dispersive spectrometer.

MCFT is both multiplex and multichannel, in that many channels are monitored simultaneously, but each channel has contributions from all wavelengths. The MCFT design spreads the light from a given Raman feature over many CCD pixels, thus reducing the SNR in comparison to a dispersive system, which puts all the light onto one (or a few) pixels. Mathematically, the MCFT interferogram is the same as that obtained with a Michelson interferometer and a shot-noise-limited detector, with the Michelson scan time equal to the integration time of the MCFT CCD. By this analogy, or more rigorously, it can be shown that $\mathrm{SNR_{MCFT}}$ has the same SNR behavior as FT-Raman, provided that both operate in the shot noise limit (Eq. 4). As indicated in Eqs. 5 and 6, the SNR may also be stated in terms of the average signal per resolution element, $\bar{L}$.

$$\mathrm{SNR_{MCFT}} = \frac{L_i}{(\Sigma L_i)^{1/2}} (A_D \Omega Q T t_M)_{MCFT}^{1/2} \tag{5}$$

$$\mathrm{SNR_{MCFT}} = \frac{L_i}{(\bar{L} N_R)^{1/2}} (A_D \Omega Q T t_M)_{MCFT}^{1/2}. \tag{6}$$

Therefore, we expect $\mathrm{SNR_{MCFT}}$ to equal $\mathrm{SNR_{FT}}$ and $\mathrm{SNR_{DIS}}$ for a single spectral line in the shot noise limit, assuming all else is equal. But $\mathrm{SNR_{FT}}$ and $\mathrm{SNR_{MCFT}}$ will decrease as the spectrum becomes more complex.[15,16] It is also important to note that ($A_D\,\Omega\,Q\,T$) can be much larger for FT and MCFT spectrometers compared to dispersive ones, and we will exploit this feature later. In addition, the MCFT will be immune to source flicker noise, while a Michelson interferometer's SNR will degrade if the laser fluctuates on a time scale comparable to the sampling interval.

CCD Uniformity Correction. MCFT has an additional "noise" source not present in FT-Raman, from variations in light distribution across the CCD. Fourier transformation of these variations yields noise across the entire Raman spectrum, in addition to possible features due to fixed pattern variation in the CCD. This issue has been addressed previously,[13] but the approach required mirror adjustment and some loss in resolution. One approach used in the present work is to block one of the split input beams to prevent interference, and record the CCD output. The resulting plot of CCD output vs. pixel number contains the response nonuniformities, both from pixel gain variation and optical transmission variation. A similar trace can be recorded with the opposite beam blocked, and the corrected interferogram may be reconstructed via Eq. A7 in the Appendix. We will show below that this procedure increases SNR by 40%. An alternative method involves only software manipulation and yields better results. Much of the noise arises from spatial frequencies outside the relevant Raman shift range. By transforming the raw interferogram, zeroing the spatial frequency components below 0.3 (corresponding to Raman shift of 4,000 to 12,755 cm^{-1} relative to 785 nm), then inverting, one reconstructs the CCD response *without* Raman information (but containing nonuniformities). In effect, the interferometer and CCD response are being corrected by using light that is not modulated at Raman frequencies. As shown in the Appendix, the raw interferogram may be corrected for response nonuniformity according to Eq. A14.

Resolution Improvement by an Optical Heterodyne. The resolution or instrumental linewidth (ILW) is determined by the maximum light path difference. By analogy to the Michelson interferometer,[17] the ILW ($\Delta\sigma$) for triangle apodization is

$$\Delta\sigma = \frac{1.8}{2\alpha \sin\theta_{max}} \tag{7}$$

where θ_{max} is the largest acceptance angle for a double-sided interferogram, and α is $1/\sqrt{2}$ (see Appendix). To avoid aliasing, the Nyquist wavenumber σ_N must exceed the laser frequency σ_L and it is given by

$$\sigma_N = \frac{N}{4\alpha \sin \theta_{max}} \geq \sigma_L. \quad (8)$$

Equation 8 sets a maximum value for α and limits the ILW to

$$\Delta\sigma = \frac{3.6}{N}\sigma_N \geq \frac{3.6}{N}\sigma_L. \quad (9)$$

Both SNR and ILW considerations favor NIR laser excitation, since smaller σ_L yields smaller $\Delta\sigma$. For a 784-nm laser excitation and a 2000-channel detector, $\sigma_L = 12{,}755$ cm^{-1}, $N = 2000$, and ILW ≥ 23 cm^{-1}.

Equation 9 indicates that the resolution can be improved by either increasing N or reducing σ_N. Since the interferogram is symmetric around the centerburst, an effective increase of N can be achieved by collecting a single-sided interferogram, instead of a double-sided one, and using the data reflection algorithm (DRA) to generate a double-sided interferogram with more points.[6,18] Alternatively, the same effect can be achieved by phase correction when performing the FT. If the centerburst is located at channel number $x = 1700$, then N can be effectively increased to 3400, and the theoretical ILW is reduced to 13.5 cm^{-1}.

Although reducing the Nyquist frequency below the laser line is achievable by aliasing,[12] this method quickly diminishes the SNR and hence is not feasible for Raman spectroscopy. Tilting the CCD can reduce aliasing,[10] but it does not change the fact that the pixel is wider than the interference fringe, and hence it also worsens the SNR. Several optical heterodyning configurations have been proposed to reduce the apparent frequency of Raman features. Dohi and Suzuki used reflective gratings,[19] Okamoto et al. used a tilted optical flat to create a variable-path difference for different wavelengths,[20] and Barnes et al. used a Moiré fringe technique.[12] The configuration we are proposing here, which is shown in Fig. 1, is also based on Moiré fringes, but the concept is somewhat simpler. It preserves both the frequency linearity and the large sample size capability of MCFT while improving its resolution.

For an extended light source, in order for the interferogram to maintain large modulation depth, the CCD must be located exactly at the focal plane of the FT lens. The most straightforward way of heterodyning is to project a sinusoidal interferogram on the CCD to create a beat frequency. As shown in Fig. 2, this step may be achieved by putting an imaging lens **14** in front of the beamsplitter and a holographic transmission grating at the object plane of this lens. The conjugation ratio of the FT lens **18** and lens **14** determines the ratio of the spatial frequency of the beating wave f_0 to that of the grating f_G.

$$\frac{f_0}{f_G} = \frac{FL_{14}}{FL_{18}}. \quad (10)$$

The original interferogram S and the beating wave S_0 are written as follows, with f representing an individual spatial frequency:

$$S(x) = \sum_{j=1}^{N/2} S_j[1 + \cos(2\pi f_j x)] \qquad x = 1 \text{ to } N \quad (11)$$

$$S_0(x) = S_0[1 + \cos(2\pi f_0 x)]. \quad (12)$$

Multiplication of the signal and grating image yields

$$S(x)\cdot S_0(x) = S_0 \sum_{j=1}^{N/2} S_j \left[1 + \cos 2\pi f_0 x + \cos 2\pi f_j x + \frac{1}{2}\cos 2\pi(f_j + f_0)x + \frac{1}{2}\cos 2\pi(f_j - f_0)x\right]. \quad (13)$$

In the last term the original spatial frequency f_j is heterodyned to $(f_j - f_0)$. The heterodyned Nyquist spatial frequency 0.5 now corresponds to unheterodyned spatial

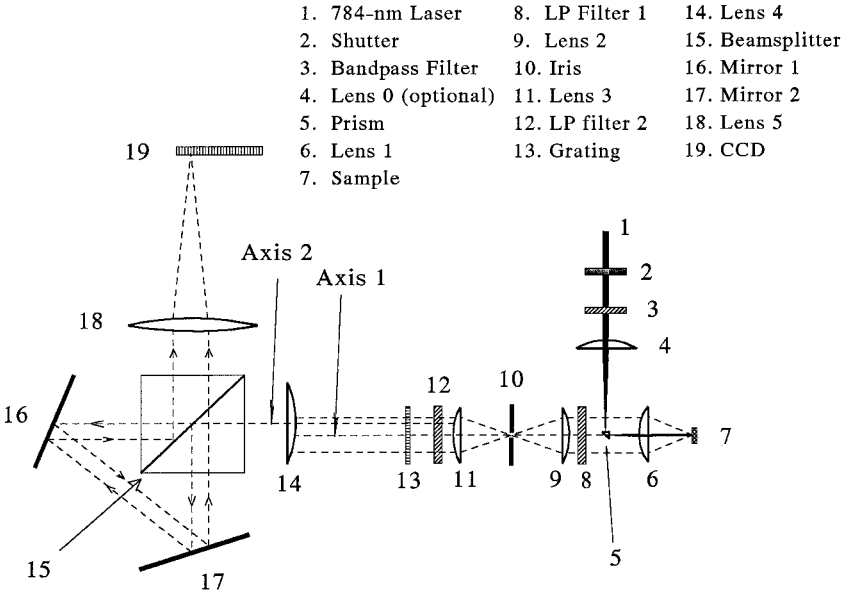

FIG. 1. Optical layout of the MCFT Raman spectrometer.

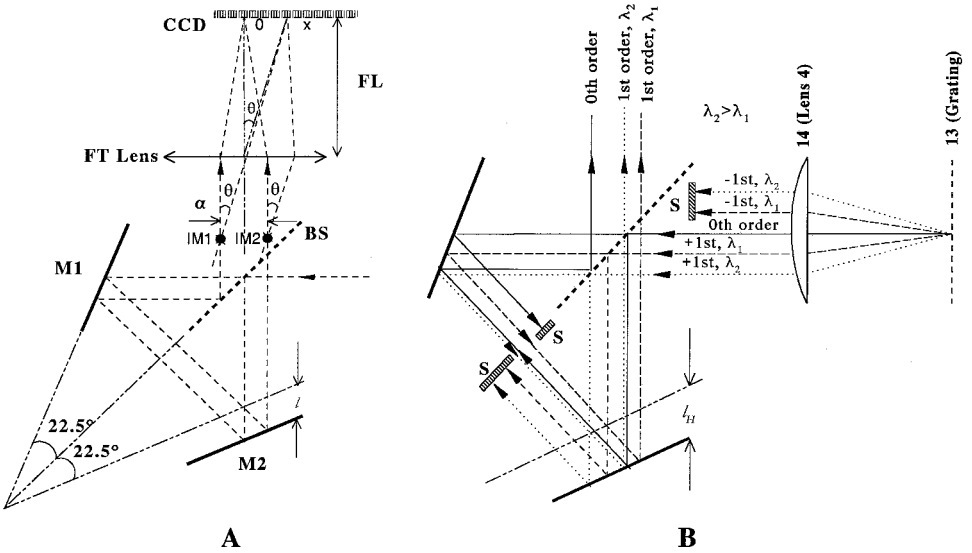

FIG. 2. Principle of the triangle Sagnac interferometer for unheterodyned (**A**) and heterodyned (**B**) operation. (**A**) **BS**, beamsplitter; **M1** and **M2**, mirrors; **IM1** and **IM2**, the two virtual images of the source (their actual position are between the two mirrors, but they are shown here for convenience); α, the space between the two images; *l*, displacement of **M2**. "0" position on the CCD represents the centerburst of the interferogram. (**B**) Optical heterodyning illustrated in diffraction. **S** indicates optical stops used to eliminate unwanted heterodyned frequency components.

frequency $0.5 + f_0$, and if the mirror **17** is readjusted so that this corresponds to the laser frequency, then l and α are increased by a factor of $(1 + 2f_0)$, and, following Eq. 7, the ILW is decreased by the same factor, so that

$$\Delta\sigma_H = \frac{3.6}{N(1 + 2f_0)}\sigma_L. \qquad (14)$$

For the conditions used here, $\Delta\sigma_H$ equals 10.3 cm^{-1} for $f_0 = 0.613$ ($N = 2000$) and 6 cm^{-1} when DRA and phase correction are applied ($N = 3400$).

Due to the presence of the other terms in the bracket of Eq. 13, f_0 must be carefully chosen to avoid frequency overlapping of different terms in the Fourier transformed spectrum. Even if this can be done, these terms still contribute a great deal of noise to the Raman spectrum. Fortunately, the design allows these terms to be eliminated and the heterodyned spectrum to be isolated on the CCD. This can be achieved when f_G is high enough to ensure that the images formed by the 0th-order and 1st-order diffraction can be well separated in space. As demonstrated in Fig. 2B, one can physically block the 1st-order diffraction of the clockwise traveling beam and the 0th-order and −1st-order diffraction of the counter clockwise traveling beam, so that only the 0th order of one beam and the +1st order of the other remain to interfere. The result is a pure heterodyned interferogram on the CCD.

EXPERIMENTAL

An optical layout of the MCFT Raman spectrometer is shown in Fig. 1. The triangle Sagnac interferometer consists of a cubic beamsplitter **15** and two mirrors, **16** and **17**, all in fixed positions. A converging light beam enters the interferometer from the collection optics and is split into two halves by the beamsplitter. The interferogram is imaged onto **19**, a CCD detector (Spex "Spectrum One Standard") by a Fourier transform lens **18**. The CCD chip has 2000 × 800 pixels, and each pixel is 15 μm × 15 μm. The CCD temperature was maintained at −130 °C, and the vertical pixels were binned to yield 2000 superpixels. The interferogram was transferred to a 486 computer and analyzed with GRAMS and Hyperplot commercial software.

The 784-nm light source **1** was a Ti:sapphire laser pumped by an Ar-ion laser. A shutter **2** was used to control the exposure time. The laser was prefiltered by using a bandpass interference filter **3** to reject plasma lines. It was reflected by a mini-prism **5**, and focused by a lens **6** (FL = 78 mm) onto the sample. An optional lens **4** can be placed before the prism to vary the laser spot size at the sample position. The scattered light was collimated by the same lens **6**. The 784-nm and shorter wavelength components in the scattered light were filtered out by two-stage filtering optics, namely, 785-nm interference long-pass filter **8** (1 in. diameter), lens **9** (Nikon 50 mm, *f*/1.4), iris **10**, lens **11** (Nikon 50 mm, *f*/1.4), and another long-pass filter **12**. After filtering, the collimated light was then focused by a lens **14**, into the interferometer. Lens **14** was positioned in such a way that the two virtual images **IM1** and **IM2** were formed between the two mirrors (see Fig. 2). With the use of a cylindrical lens (Melles Griot, precision plano-cylindrical), focal length = 240 mm for **14**, the interferogram was focused to a horizontal stripe on the CCD, and an improvement in sensitivity was achieved. The overall collection efficiency of the spectrometer was about *f*/5.2. In order to use the data reflection algorithm or phase correction to enhance resolution without sacrificing sensitivity, lens **14** was moved off axis, so the centerburst was shifted to one side of the CCD.

Optical heterodyning was performed by using a Ronchi transmission grating (Edmund Scientific) placed at the focal plane of lens **14**, [in this case, it is a high-quality enlarging lens (Rodenstock, FL = 240 mm, *f*/5.6)]. It was essential to align the Ronchi grating lines parallel to the CCD vertical axis. The grating position was adjusted along the optical axis to generate maximum modulation depth at the CCD for a single line source.

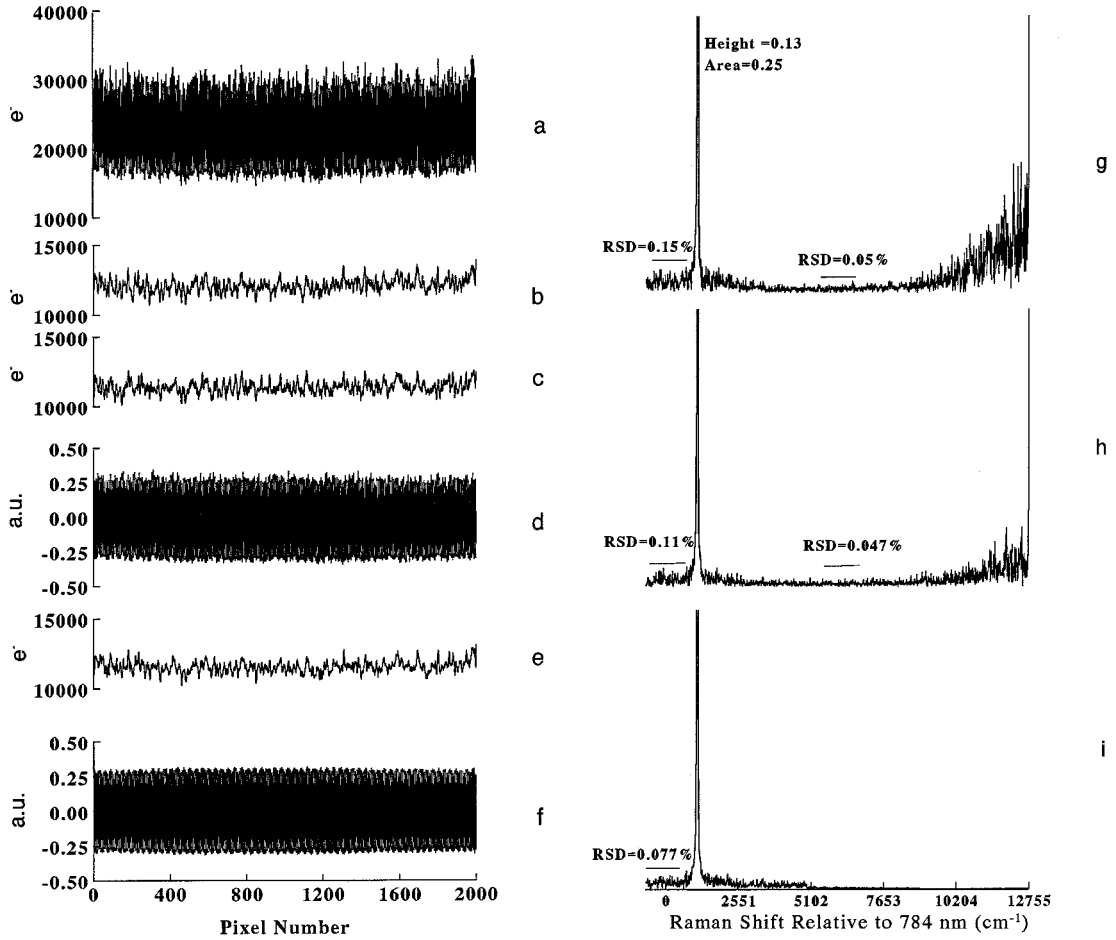

FIG. 3. Noise correction procedure to improve SNR in unheterodyned MCFT. (**a**) Raw interferogram of the HeNe laser. (**b**) Clockwise traveling beam. (**c**) Counter-clockwise traveling beam. (**d**) Noise removed interferogram following Eq. A7. (**e**) S_{DC} obtained via inverse fast Fourier transform (FFT) after deleting the frequency-domain features above 0.3. (**f**) The interferogram after SNC via Eq. A15. (**g**) Magnitude-mode FFT of the raw interferogram **a**. (**h**) FFT of d. (**i**) FFT of **f**.

The performance of the MCFT Raman spectrometer was compared to that of a multichannel dispersive Raman spectrometer, consisting of a Chromex 250IS *f*/4 spectrograph (600 L/mm, 50-μm slit), with an EEV 15-11 deep-depletion CCD in a Photometrics 270 housing. The observed ILW was about 6 cm^{-1}. The 1024-channel deep-depletion CCD is more sensitive at the working Raman wavelengths than the ISA spectrum CCD used for MCFT. A diode laser (SDL 8530) operating at 785 nm provided the Raman excitation for the dispersive spectrometer.

RESULTS AND DISCUSSION

Before SNR performance of various designs is compared, the nonuniformity correction for MCFT should be discussed. Figure 3a shows the raw interferogram of a HeNe laser line (632.8 nm). Figure 3b and 3c are the CCD output when either the clockwise beam (3b) or counter-clockwise (3c) beams are blocked in the interferometer. These patterns represent the system response in the absence of intentional interference and contain contributions from pixel gain variation, sample texture, and variations in interferometer transmission. Figure 3d is the interferogram reconstructed from 3a–3c according to Eq. A7, demonstrating an observable decrease in noise. The software noise correction (SNC) procedure is illustrated in spectra 3e, 3f, and 3i. Figure 3e is the raw interferogram from 3a after software removal of spatial frequencies above 0.3 (σ = 4500 cm^{-1}), which are those containing the Raman spectrum. Figure 3f is the interferogram reconstructed in software from 3a and 3e via Eq. A15. The effect of these procedures on SNR is shown in spectra 3g, 3h, and 3i, which are FTs of the raw and reconstructed interferograms with the vertical scale magnified to show noise. The relative standard deviation of the Raman shift region of 500–1500 cm^{-1} has been reduced by a factor of 2 after SNC. Furthermore, the software procedure (3a, 3e, 3f, and 3i) requires no beam blocking or user intervention. The SNC procedure is used for all subsequent MCFT spectra, unless noted otherwise.

The effect of SNC on a more complex spectrum is illustrated in Fig. 4, which was obtained with a neon bulb at the Raman sample position. The raw interferogram (4a) shows a varying dc level due to the more efficient light collection at the center of the interferometer axis. The reconstructed interferogram after SNC is Fig. 4b. The FT of Fig. 4a is shown in 4c, following 8× zero-filling and phase correction. Figure 4d is the FT of 4b, with both SNC and data reflection, and 4e is a dispersive/CCD spectrum for comparison. Note that the SNC procedure removes negative peak artifacts and yields a full

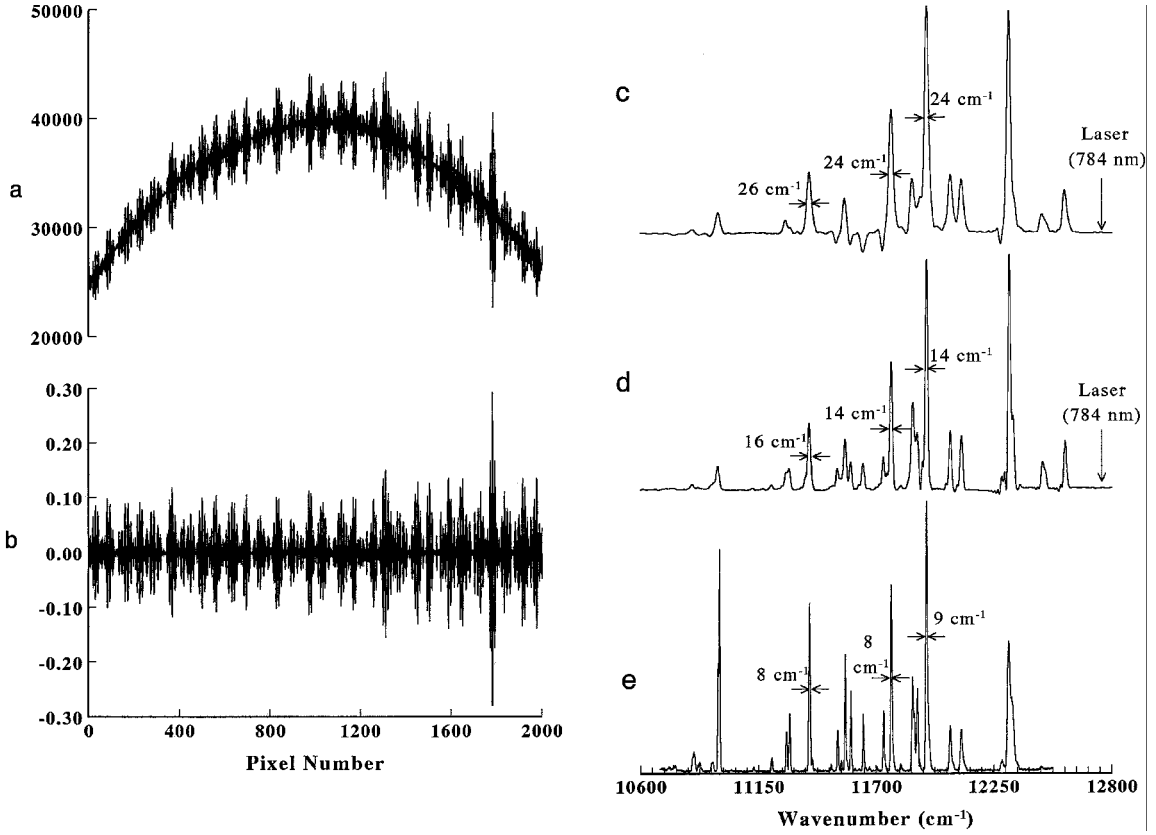

FIG. 4. Effect of SNC procedure on peak shape, and resolution test without heterodyning. (**a**) Raw interferogram of neon bulb. (**b**) Interferogram after SNC via Eq. A15. (**c**) Phase-corrected absorption-mode FFT of **a** after 8 × zero-filling. (**d**) Same as **c**, but from SNC interferogram **b**. (**e**) Spectrum taken with the dispersive system.

width at half-maximum (FWHM) of 14 cm^{-1} for the neon atomic emission lines. The theoretical FWHM for N = 3400 and σ_{max} of 12,755 cm^{-1} is 13.5 cm^{-1}, based on Eq. 7. Thus the unheterodyned MCFT spectrometer is demonstrating resolution that is close to the limiting resolution for the conditions employed.

We will measure the SNR for the dispersive system as the ratio of the peak area to the standard deviation of the peak area (i.e., the inverse of the relative standard deviation of the peak area). This is quite different from the ratio of peak height to the baseline standard deviation, which results in an erroneously high estimate of SNR for dispersive systems (since the baseline may contain little or no shot noise). For dispersive spectra, the peak area was measured 50 times to determine its mean and standard deviation. For MCFT and FT-Raman, noise is spread equally over the spectrum, so the peak height has the same standard deviation as the baseline. These effects are illustrated in Table I, which lists SNR values for several samples and conditions. Figure 5 compares spectra of a strong scatterer (naphthalene) with relatively few Raman features. For similar laser power and measurement time, the MCFT and dispersive spectra yield similar SNR values. Although the MCFT spectrum has more baseline noise, the SNRs measured correctly are comparable. Observed SNR values for several samples and conditions are shown in Table I. After adjustments for laser power and measurement time, the SNR for MCFT is generally lower than that for the dispersive system. Of course, these comparisons depend on a variety of experimental conditions, including collection optics, resolution, power density, etc.

Because MCFT combines elements of both FT-Raman and dispersive/CCD spectrometers, it retains some of the

TABLE I. SNR values for several samples and spectrometers.

	MCFT	Dispersive
Naphthalene (764 cm^{-1})	89 (n = 40)[a]	140 (n = 50)[a]
	80 (n = 40)[b]	81[b]
	100[3]	380[c,d]
	(30 mW, 5 s, 785 mm)	(120 mW, 1 s, 785 mm)
Glassy carbon (1315 cm^{-1})	103[c] (830 mm, 180 mW, 2 min)	108[b] (785 mm, 50 mW, 1 min, n = 20)
0.2 M K^2 SO_4 (980 cm^{-1})	39[b] (830 mm, 135 mW, 1 min, n = 20)	88[a] (784 mm, 50 mW, 1 min, n = 20)

[a] Mean peak area divided by standard deviation (SD) of peak area; n = number of runs.
[b] Mean peak height/SD of peak height.
[c] Mean peak height/SD of baseline.
[d] Assessment of SNR as mean peak height over the SD of the baseline can seriously overestimate the SNR for dispersive systems.

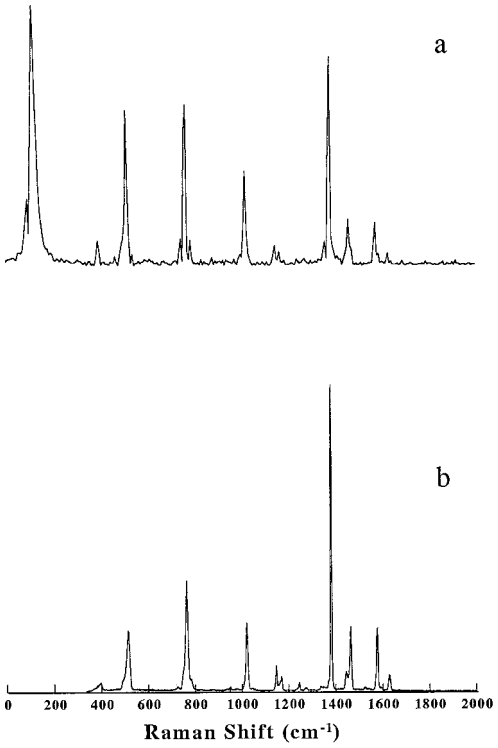

FIG. 5. (**a**) Naphthalene Raman spectrum taken with MCFT, 784-nm laser, 200 mW, and 1-s integration time. (**b**) Spectrum taken with the dispersive spectrometer with a red-enhanced CCD, 784-nm laser, 130 mW, and 1-s integration.

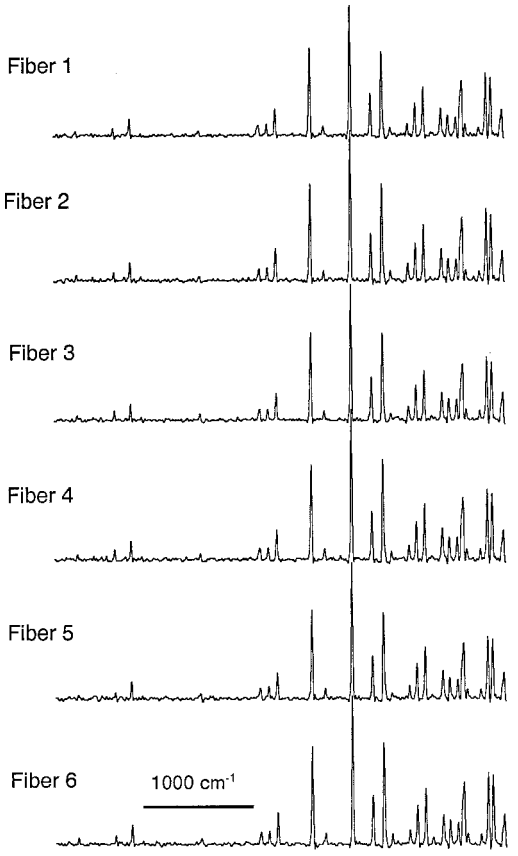

FIG. 6. Demonstration of the multitrack detection ability of the MCFT spectrometer with a cylindrical lens and a six-fiber array carrying light from the same neon bulb source. Six strips of interferograms were well separated on the CCD. The long-pass filters were not used, and the Nyquist frequency was set at 13,336 cm^{-1}.

advantages of both. First, MCFT can operate in "multitrack" mode, like some dispersive/CCD systems, in which several samples can be monitored simultaneously. A line of fibers carrying Raman light can be positioned vertically at the sample position in Fig. 1 and imaged onto the CCD. An interferogram will result from each fiber and can be processed to yield a spectrum. Figure 6 shows an example, when six optical fibers monitored a neon bulb. Since the cylindrical lens (lens **4**) compresses the interference pattern vertically on the CCD, crosstalk is minimal. A second advantage of MCFT is the high $A_D\Omega$ product, which can be used to reduce laser power density or sample a large area, or both. Figure 7 shows MCFT and dispersive spectra of cobalt phthalocyanine. The laser was focused for the dispersive case, in order to image the laser spot (~ 50 μm) onto the entrance slit (also 50 μm), and the sample was degraded. An unfocused beam covering ~ 1 mm yielded a useful spectrum with MCFT with no observable sample damage. The large $A_D\Omega$ of MCFT is also useful for a sample contained in an integrating sphere. The MCFT system can monitor a relatively large hole in a sphere, thus collecting a fairly large fraction of multiply reflected light. Figure 8 shows a factor of 13 increase in signal for a liquid sample placed in a 1.5-cm-diameter sphere, compared to one in a 1-cm quartz cuvette. A third MCFT advantage is the inherent frequency stability of FT instruments. Since the entire interferogram is analyzed to determine the frequency, there is no concern about errors in grating position. The experiment depicted in Fig. 4 was repeated 26 times over a period of 12 days, yielding standard deviations of peak frequencies of 0.44 and 0.27 cm^{-1} for peaks at 11,771.13 and 11,936.58 cm^{-1}. One month later, the same neon lines were located at 11,770.9 and 11,936.8 cm^{-1}, well within the range observed over twelve days. Since the laser line also appears on the MCFT spectrum, the precision of Raman shift could be even better when internally referenced to the laser frequency.

The optical heterodyne technique described in the Theory section was implemented experimentally by placing an 80-line/mm Ronchi grating as shown in Fig. 1. If no adjustment is made to the position of **M2**, the normal and heterodyned spectra of Fig. 9a and 9b result. Note the fundamental HeNe line at 15,803 cm^{-1} absolute cm^{-1} plus the difference frequency at 1356 absolute cm^{-1}. In addition, the aliased sum frequency appears at 6076 cm^{-1}. If **M2** is displaced further to improve resolution, aliasing becomes more severe, and it becomes difficult to separate the sum, difference, and fundamental frequencies. Fortunately, this problem can be solved by placing masks as shown in Fig. 2B. First, only the 0 and +1 diffraction orders from the Ronchi grating are allowed to enter the interferometer. Second, a mask between **M1** and **M2** limits the interference to that between the 0th-order light (counter clockwise) and +1 order (clockwise). The result is that *only* the difference frequency is projected onto the CCD and detected, as shown in Fig. 9c. Figure 9d is an expansion of the difference frequency region for a sample of Tylenol® (4-acetamidophenol) following calibration

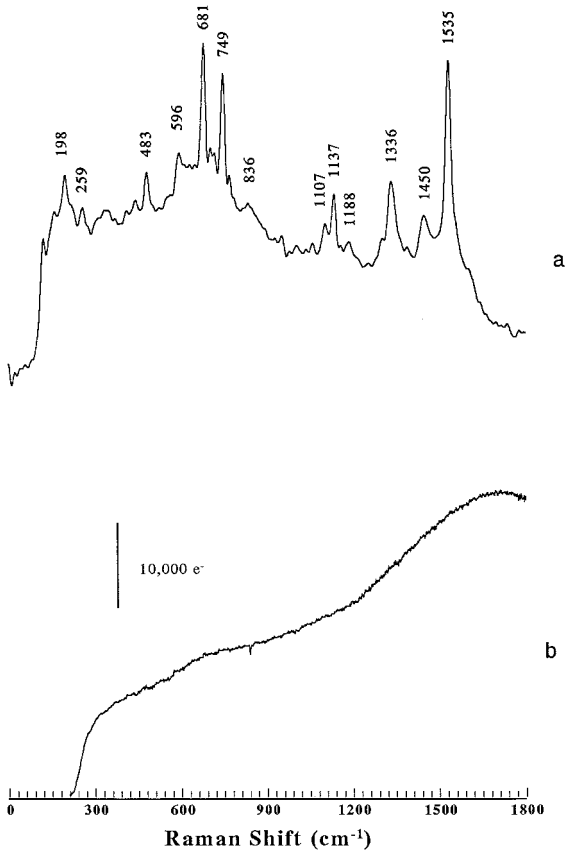

FIG. 7. Raman spectra of cobalt phthalocyanine powder in air. (**a**) Spectrum taken with the MCFT, 100-mW laser power, spot size of about 2 mm in diameter, and 1-min integration. (**b**) Spectrum taken with the dispersive spectrometer, 50 mW focused to ~ 50 μ, and 0.5-s integration.

against a Raman shift standard,† and 9e is an unheterodyned MCFT spectrum. The linewidth for the 1168-cm^{-1} line of Tylenol® decreased from 15.5 to 8 cm^{-1} when the optical heterodyne was employed. Table II summarizes the theoretical and observed linewidths for several MCFT configurations. Recall that, in all MCFT cases, linewidths do not vary when the input aperture is increased.

In the configuration yielding the spectra of Fig. 9, the heterodyne technique causes a significant loss of signal and SNR, due mainly to the Ronchi grating. A square wave transmission grating generates many diffraction orders, but only one (+1) was analyzed to produce spectrum 9d. The Ronchi grating diffracted about 3% of a laser beam into the +1st order when measured with a power meter. An ideal sinusoidal grating would theoretically diffract 50% of the incident light into the +1st order, so significant improvement in efficiency should be possible with a custom grating. In the best case, a heterodyned spectrum should have $1/\sqrt{2}$ the SNR of the nonheterodyned case.

Finally, it is worthwhile to consider how MCFT spectra can be compared to existing dispersive spectra, for purposes of compound identification, library searching, etc. The spectral response correction discussed elsewhere[21] corrects the relative peak intensities for CCD response variation with wavelength, filter transmission,

† 4-Acetamidophenol, ASTM standard E 1848.

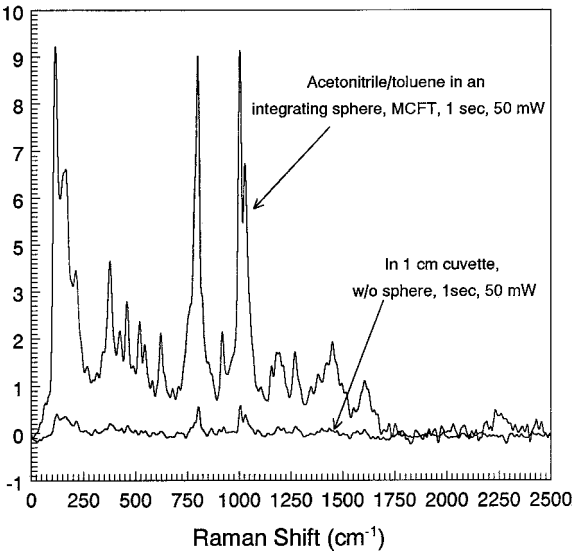

FIG. 8. Utilization of an integrated sphere as a liquid sample holder to enhance the signal for the MCFT Raman spectrometer. A quartz sphere with 1.5-cm inside diameter was coated with silver on its exterior.

etc., so corrected MCFT spectra should have relative intensities comparable to those obtained with other spectrometers using 785-nm lasers. Of course, there will still be peak height variations between instruments operating with different instrumental linewidths. A test of the similarity of MCFT and dispersive spectra was provided by searching a 300-spectra dispersive library for a match to an MCFT spectrum, with all spectra corrected for instrument response. As shown in Fig. 10, the first "hit" from the library search correctly matched the MCFT "unknown", despite the difference in MCFT instrumental linewidth (14 cm^{-1}) and the linewidth used to collect the library (6 cm^{-1}).

CONCLUSION

The combination of shot-noise-limited CCD detectors and the Sagnac interferometer provides MCFT with many of the benefits of both dispersive/CCD Raman and FT-Raman. These benefits are accompanied by a fundamental change in SNR characteristics that affects the way MCFT might be applied. As always, the choice among dispersive, FT-Raman, and MCFT is governed by the application. MCFT provides an attractive alternative to existing Raman techniques in several situations. First, the high $A_D\Omega$ of MCFT may be useful for sampling relatively large sample areas or volumes, such as dilute solutions or samples contained in an integrating sphere. Second, the large $A\Omega$ permits low laser power density, in cases where sample damage or regulatory limits are issues. Third, MCFT provides full spectral coverage with frequency precision and stability, an important property for situations when continuous monitoring or spectral subtraction and/or multivariate calibrations are involved. Finally, the lack of moving parts and simple optical layout make the MCFT spectrometer relatively rugged and possibly inexpensive if offered commercially.

As discussed in some detail, the SNR for MCFT will generally lie between that of FT-Raman and a dispersive/

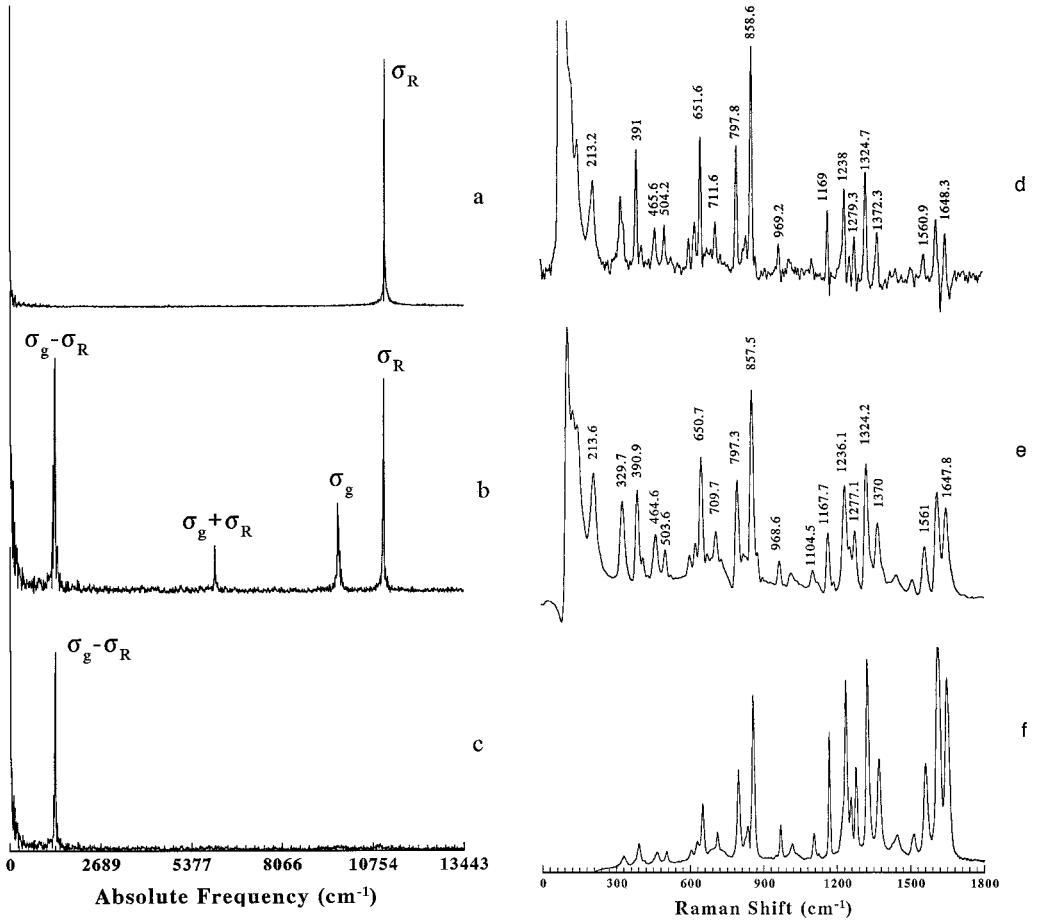

FIG. 9. Improving the resolution via optical heterodyning. (**a**) Spectrum of HeNe laser without heterodyning. The real frequency σ_R is 15803 cm^{-1} but appears at 11083 cm^{-1} due to aliasing. (**b**) The heterodyned spectrum without the optical stops. σ_R appears at the same position, σ_g is the beating frequency generated by the grating, and $\sigma_g + \sigma_R$ is the sum of the two. All three are aliased, but the difference, $\sigma_g - \sigma_R$, is not. (**c**) Spectrum with optical stops inserted as shown in Fig. 2B. (**d**) MCFT Raman spectrum of Tylenol® heterodyned with an 80-line/mm Ronchi grating. **M2** was displaced further to increase resolution. (**e**) MCFT Raman spectrum of Tylenol® without heterodyning. (**f**) Tylenol® Raman spectrum taken with the dispersive spectrometer.

CCD system, for comparable laser power, measurement time, and sampling optics. SNR_{MCFT} will be comparable to SNR_{FT} if both systems operate in the shot noise limit. Since FT-Raman systems often have high detector noise, SNR_{FT} will often be less than SNR_{MCFT} due to contributions from detector noise. In many practical situations (particularly with high background) SNR_{DIS} will significantly exceed SNR_{MCFT}.

Although the heterodyne technique reduces the instrumental linewidth to a value similar to many natural Raman linewidths, MCFT resolution will rarely equal or exceed those of typical dispersive and FT-Raman spectrometers. This limitation is imposed mainly by the maximum number of CCD detector elements (2000 in the present case) and will not improve without further evolution in CCD technology. The cost of 2000 × 800 CCDs

TABLE II. Resolution improvement of MCFT.

	Predicted FWHM (cm^{-1})	Observed FWHM (cm^{-1})
Unheterodyned[a]		
N = 1024, no DRA	43[b]	48 (naphthalene, 830-nm laser)[c]
N = 1024, DRA	24[b]	27 (naphthalene, 830-nm laser)
N = 2000, no DRA	24	24 (neon)[c]
N = 2000, DRA and phase corrected	14	14 (neon)
N = 2000, DRA and phase corrected	14	15.5 (Tylenol®)[c]
Heterodyned		
N = 2000, no DRA	11	11.1 (Tylenol®)
N = 2000, DRA and phase corrected	6	8 (Tylenol®)

[a] N is the number of CCD pixels along the axis of the interferogram.
[b] The predicition in Ref. 6 did not consider the broadening by a factor of 1.8 caused by triangle apodization during Fourier transform. The predicted values listed here include this factor.
[c] Naphthalene (764 cm^{-1}) and Tylenol® (1168 cm^{-1}) values are from Raman spectra; neon values are from direct monitoring of neon bulb (absolute wavenumber = 11,937 and 11,771 cm^{-1}).

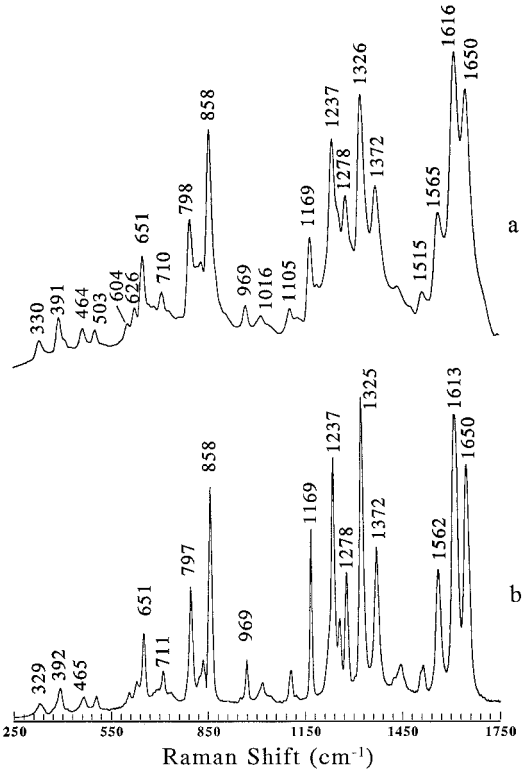

FIG. 10. Spectrometer response-corrected spectra of 4-acetamidophenol (Tylenol®) from MCFT (**a**) and dispersive (**b**) spectrometers. Spectrum **b** was the first "hit" when a dispersive library of 300 compounds was searched for a match to the MCFT spectrum. Variations in relative intensities are likely due to the differences in spectral resolution.

is likely to continue to decrease, however, due to a higher volume of CCD production. With current prices, the cost of a complete MCFT spectrometer is comparable to that of a dispersive/CCD system with similar specifications. The major expenses are in the CCD and laser, and the cost of these items will likely decrease with time, since both the CCD and laser are solid-state devices amenable to volume production.

ACKNOWLEDGMENTS

This work was supported by an STTR grant from the National Science Foundation to Chromex, Inc. and The Ohio State University. The assistance of Professor Morris Kagan of the OSU Physics Department was appreciated.

APPENDIX

The Sagnac interferometer functions in a source-doubling mechanism. As shown in Fig. 2A, two identical images **IM1** and **IM2** are formed by the beamsplitter **BS** and the two mirrors **M1** and **M2**. When the two mirror planes both form 22.5° angles with the beamsplitter plane, the line connecting the two images is perpendicular to the optical axis of the Fourier lens. At this configuration, the distance α between the two images is related to the displacement of the mirror **M2**, referred to as l,[14] by

$$\alpha = l\sqrt{2}. \tag{A1}$$

The path difference at angle θ is $\alpha\sin\theta$. Let E_i denote the electric field created by the ith image, $i = 1, 2$; then at any time t,

$$E_1(\theta) = e_1(\theta)\cos(\omega t + \varphi)$$

$$E_2(\theta) = e_2(\theta)\cos\left(\omega t + \varphi + \frac{2\pi\alpha \sin\theta}{\lambda}\right) \tag{A2}$$

the light intensity inserted by the two images separately is

$$I_i(\theta) = \langle E_i^2\rangle = \frac{1}{2}e_i^2(\theta) \qquad i = 1, 2. \tag{A3}$$

When interference occurs, the total intensity is

$$I(\theta) = \langle (E_1 + E_2)^2\rangle$$

$$= [I_1(\theta) + I_2(\theta)] + 2\sqrt{I_1(\theta)I_2(\theta)}\cos\left(\frac{2\pi\alpha \sin\theta}{\lambda}\right). \tag{A4}$$

The detected signal, $S(\theta)$, however, is the product of the light intensity and quantum efficiency Q of the individual pixels. Thus,

$$S_i(\theta) = I_i(\theta)Q(\theta), \qquad i = 1, 2. \tag{A5}$$

and

$$S(\theta) = I(\theta)Q(\theta)$$

$$= [S_1(\theta) + S_2(\theta)] + 2\sqrt{S_1(\theta)S_2(\theta)}\cos\frac{2\pi\alpha \sin\theta}{\lambda}. \tag{A6}$$

The above equation suggests that the interferogram is complicated by the angular distribution of light intensity, such as that arising from sample texture, and by the pixel quantum efficiency nonuniformity. Usually sample texture will introduce low-frequency noise that is well separated from Raman signal and therefore is not much of concern; however, the FT of the second term in A6 will cause this noise to be convoluted into the Raman signal region, thus decreasing the SNR. Equation A6 also points out a way to solve these problems. Suppose $S_1(\theta)$ and $S_2(\theta)$ can be collected separately; then one can subtract $[S_1(\theta) + S_2(\theta)]$ out of $S(\theta)$ and divide the result by $2\sqrt{S_1(\theta)S_2(\theta)}$. The corrected interferogram S_C will have the form

$$S_C(\theta) = \frac{S(\theta) - [S_1(\theta) + S_2(\theta)]}{2\sqrt{S_1(\theta)S_2(\theta)}} = \cos\frac{2\pi\alpha \sin\theta}{\lambda}. \tag{A7}$$

The case becomes more complicated when multiple wavelengths are added together. Both I and Q will be functions of θ as well as λ. Thus

$$S_i(\theta) = \sum_\lambda I_i(\lambda, \theta)Q(\lambda, \theta), \qquad i = 1, 2 \tag{A8}$$

and

$$S(\theta) = [S_1(\theta) + S_2(\theta)] + \sum_\lambda 2\sqrt{I_1(\lambda, \theta)I_2(\lambda, \theta)}Q(\lambda, \theta)$$

$$\times \cos\frac{2\pi\alpha \sin\theta}{\lambda}. \tag{A9}$$

Now it is only possible to correct the noise due to the dc component, namely, the first term in 0 Eq. A9. The difficulty arises from the fact that the second term can no

longer be expressed as a function of S_1 and S_2. However, if it is possible to separate the two factors λ and θ, so that

$$I_i(\lambda, \theta) = I_i(\lambda)\cdot\delta I_i(\theta) \qquad i = 1, 2$$
$$Q(\lambda, \theta) = Q(\lambda)\cdot\delta Q(\theta) \tag{A10}$$

then the second term becomes

$$2\left\{\sum_{\lambda}\sqrt{I_1(\lambda)I_2(\lambda)}\,Q(\lambda)\cos\frac{2\pi\alpha\,\sin\theta}{\lambda}\right\}\sqrt{\delta I_1(\theta)\delta I_2(\theta)}\cdot\delta Q(\theta) \tag{A11}$$

and the geometric average of S_1 and S_2 is

$$\sqrt{S_1(\theta)S_2(\theta)} = \sqrt{\sum_{\lambda}[I_1(\lambda)Q(\lambda)]\cdot\sum_{\lambda}[I_2(\lambda)Q(\lambda)]} \times\sqrt{\delta I_1(\theta)\delta I_2(\theta)}\cdot\delta Q(\theta). \tag{A12}$$

Now, divide the second term by $2\sqrt{S_1(\theta)S_2(\theta)}$; the result is

$$\frac{\sum_{\lambda}\sqrt{I_2(\lambda)I_2(\lambda)}\cdot Q(\lambda)}{\sqrt{\sum_{\lambda}[I_1(\lambda)Q(\lambda)]\cdot\sum_{\lambda}[I_2(\lambda)Q(\lambda)]}}\cdot\cos\frac{2\pi\alpha\,\sin\theta}{\lambda}. \tag{A13}$$

This way, the angular nonuniformity of the light distribution and the quantum efficiency can still be corrected.

To make this noise correction procedure practical, we may think that if the beamsplitter and the FT lens were perfect, then S_1 and S_2 in Eq. A6 would be the same and would be equal to $S_{dc}/2$; in this case, Eq. A6 becomes

$$S(\theta) = S_{DC}(\theta) + S_{DC}(\theta)\cos\frac{2\pi\alpha\,\sin\theta}{\lambda}. \tag{A14}$$

S_{dc} can be obtained without physically collecting S_1 and S_2. One can just delete the high-frequency components from the fast Fourier transform of S, do an inverse FFT, and use the result as S_{dc}. Then, S_C can be obtained via the following equation:

$$S_C(\theta) = \frac{S(\theta) - S_{DC}(\theta)}{S_{DC}(\theta)}. \tag{A15}$$

Figure 3i shows that this software noise correction method works just as well.

1. P. J. Hendra, "Fourier Transform Raman Spectroscopy", in *Modern Techniques in Raman Spectroscopy*, J. J. Laserna, Ed. (John Wiley and Sons, London, 1996), pp. 73–108.
2. D. B. Chase, Anal. Chem. **59,** 881A (1987).
3. P. Hendra, C. Jones, and G. Warnes, *FT-Raman: Instrumentation and Chemical Application* (Ellis Harwood, New York, 1991).
4. R. L. McCreery, "CCD Array Detectors for Multichannel Raman Spectroscopy", in *Charge Transfer Devices in Spectroscopy*, J. Sweedler, K. Ratzlaff, and M. Denton, Eds. (VCH, New York, 1994), pp. 227–279.
5. R. L. McCreery, "Instrumentation for Dispersive Raman Spectroscopy", in *Modern Techniques in Raman Spectroscopy*, J. J. Laserna, Ed. (John Wiley and Sons, London, 1996), Chap. 2.
6. J. Zhao and R. L. McCreery, Appl. Spectrosc. **50,** 1209 (1996).
7. G. W. Stroke and A. Funkhouser, Phys. Lett. **16,** 272 (1965).
8. H. Aryamanya-Mugisha and R. R. Williams, Appl. Spectrosc. **39,** 693 (1985).
9. M. Hashimoto and S. Kawata, Appl. Opt. **31,** 6096 (1992).
10. S. Takahashi, J. S. Ahu, S. Asaka, and T. Kitagawa, Appl. Spectrosc. **47,** 863 (1993).
11. T. Okamoto, S. Kawata, and S. Minami, Appl. Opt. **23,** 269 (1984).
12. T. H. Barnes, T. Eiju, and K. Matsuda, Appl. Opt. **25,** 1864 (1986).
13. J. Sweedler, R. Jalkian, G. Sims, M. B. Denton Appl. Spectrosc. **44,** 14 (1990).
14. J. V. Sweedler and M. B. Denton, Appl. Spectrosc. **43,** 1378 (1989).
15. N. Everall and J. Howard, Appl. Spectrosc. **43,** 778 (1989).
16. C. Brennan and I. Hunter, Appl. Spectrosc. **49,** 1086 (1995).
17. A. G. Marshall and F. R. Verdum, *Fourier Transforms in NMR, Optical, and Mass Spectroscopy* (Elsevier, New York, 1990), p. 49.
18. M. Gorshkov, and R. T. Kouves, Anal. Chem. **67,** 3412 (1995).
19. T. Dohi, and T. Suzuki, Appl. Opt. **10,** 1137 (1971).
20. T. Okamoto, S. Kawata, and S. Minami, Appl. Opt. **24,** 4221 (1985).
21. K. Ray and R. L. McCreery, Appl. Spectrosc. **51,** 108 (1997).